ADVANCED ENERGY MATERIALS
www.advenergymat.de

Effects of Grain Boundaries and Surfaces on Electronic and Mechanical Properties of Solid Electrolytes

*Weihang Xie, Zeyu Deng, Zhengyu Liu, Theodosios Famprikis, Keith T. Butler, and Pieremanuele Canepa**

Extended defects, including exposed surfaces and grain boundaries (GBs), are critical to the properties of polycrystalline solid electrolytes in all-solid-state batteries (ASSBs). These defects can alter the mechanical and electronic properties of solid electrolytes, with direct manifestations in the performance of ASSBs. Here, by building a library of 590 surfaces and grain boundaries of 11 relevant solid electrolytes—including halides, oxides, and sulfides— their electronic, mechanical, and thermodynamic characteristics are linked to the functional properties of polycrystalline solid electrolytes. It is found that the energy required to mechanically "separate" grain boundaries can be significantly lower than in the bulk region of materials, which can trigger preferential cracking of solid electrolyte particles in the grain boundary regions. The brittleness of ceramic solid electrolytes, inferred from the predicted low fracture toughness at the grain boundaries, contributes to their cracking under local pressure imparted by lithium (sodium) penetration in the grain boundaries. Extended defects of solid electrolytes introduce new electronic interfacial states within bandgaps of solid electrolytes. These states alter and possibly increase locally the availability of free electrons and holes in solid electrolytes. Factoring effects arising from extended defects appear crucial to explain electrochemical and mechanical observations in ASSBs.

1. Introduction

With the widespread adoption of rechargeable batteries in electric vehicles, laptops, and mobile phones, energy storage devices with high energy and power densities are currently needed.[1–3] For example, in ASSBs, the energy density can be potentially increased by replacing graphite with a metallic anode, such as lithium (Li) or sodium (Na).[4] Moreover, in ASSBs, the safety of the electrochemical cell is increased by replacing the flammable liquid electrolyte with non-flammable solid electrolytes (SEs).[5–7]

In the context of ASSBs, considering that the bulk moduli of ceramic SEs are typically at least twice that of Li or Na metals, it was postulated that Li or Na metal penetration can be suppressed by sufficiently stiff ceramic SEs.[6,8,9] However, this criterion is not strictly applicable to polycrystalline SEs, where Li filament propagation is still observed.[10–12] In this work, the metal deposition inside SEs will be referred to as Li ingress/penetration or Li filament. Furthermore, the critical current density—the largest current density before Li ingress is triggered—of SEs is still not satisfactory compared with commercial liquid electrolytes.[11,13–17]

Extended defects, such as exposed surfaces created by microcracks or pores, as well as GBs, are ubiquitous in ceramic polycrystalline SEs.[6,18–21] Therefore, understanding complex phenomena involving surfaces and interfaces in ASSBs appears crucial. Nevertheless, the buried nature of GBs and surfaces in fully assembled ASSBs complicates their investigations enormously, requiring the implementation of specialized tools that can provide spatially resolved information on interfacial

W. Xie, Z. Deng, Z. Liu, P. Canepa
Department of Materials Science and Engineering
National University of Singapore
9 Engineering Drive 1, Singapore 117575, Singapore
E-mail: pcanepa@nus.edu.sg

T. Famprikis
Faculty of Applied Sciences
Delft University of Technology
Delft 2628, The Netherlands

K. T. Butler
Department of Chemistry
University College London
Gower Place, London WC1E 6BT, UK

P. Canepa
Department of Electrical and Computer Engineering
University of Houston
Houston, TX 77204, USA

The ORCID identification number(s) for the author(s) of this article can be found under https://doi.org/10.1002/aenm.202304230

DOI: 10.1002/aenm.202304230

phenomena, which are often masked by overwhelmingly strong signals from the bulk and the other battery components.[22–25]

First-principles models as a base for multiscale models can provide an informed assessment of extended defects in SEs mimicking the conditions of ASSBs. For example, modeling elucidates the causal link between the observed electronic conductivity and the availability of GBs, interfaces, and exposed surfaces in SEs.[26–28]

Microcracks in SEs can lead to a concentration of stresses, while GBs are believed to be the source of initial cracks due to their low fracture toughness compared to their respective bulks.[29,30] For example, Vishnugopi et al. [31] revealed that a steep increase in local strain near GBs can cause mechanical failure of SEs. Using a phase-field model, Yuan et al.[32] investigated Li penetration in the SE $Li_7La_3Zr_2O_{12}$ (LLZO) and claimed that the mechanical forces (from stacking pressure) and the driving forces of mechanical and electrochemical origin may promote Li penetration into GB or pre-existing cracks in the SE. Ning et al.[33] claimed to observe the propagation of Li filament in argyrodite, suggesting that the ingress of Li into the available pores may widen and propagate cracks in the SE.

The unwanted problematic nucleation and growth of Li(Na) filament have been tentatively linked to changes in electronic leakage in SEs, which could be caused by inhomogeneous electronic conductivity in SEs' microstructure, for example, changes in electronic conductivity from bulk to grain boundaries and exposed surfaces.[12,16,28,34,35] At the electronic structure level of SE materials, the availability of GBs or exposed surfaces may introduce interfacial states, contributing to local changes in electronic conductivity.[28,34,36–38] The undesired electronic conductivity may cause the Li/Na ion in SE to be reduced to metal Li/Na, leading to local metal nucleation and subsequent growth and propagation.[10,11,16,39] For example, Zhu et al.[35] claimed to have observed the growth of Li filament in the GB regions of aluminum (Al)-stabilized LLZO, which they explained by an increase in the electron concentration gradient in the GB regions, which, in turn, could "attract" Li-ions nucleating Li-metal filaments in these regions. Through scanning electron microscopy, energy-dispersive X-ray spectroscopy, and Auger spectroscopy, Cheng et al.[40] claimed to directly observe the preferential deposition of Li metal in GBs in Al-doped LLZO. Using in situ electron energy loss spectroscopy, Liu et al.[41] studied the GB region of LLZO, and observed a reduction of the electronic bandgap around the GB region to ≈1 eV. The measured bandgap appears to be as low as 16% of that of LLZO bulk,[41] suggesting that Li may reduce around the more electronically conductive GBs and even initiate nucleation of Li filament.[16] Han et al.[11] suggested that changes in the electronic conductivity of LLZO are the reason leading to metal filament formation and pointed out the importance of investigating extended defects as possible origins for the high electronic conductivity.

Therefore, understanding the effects of concentrations of extended defects, such as GBs and surfaces in SEs, on their macroscopic properties appears crucial to: i) address the mechanical stability of polycrystalline SEs; ii) understand the root cause of electronic conductivity in SE materials;[42] and iii) explain how these extended defects impact the nucleation and growth of Li(Na) filaments. To address the effects of extended defects on the mechanical and electronic properties of polycrystalline SEs, we build accurate surface and GB models of topical SEs, including oxides, sulfides, phosphates, and halides. These models give insights into the variations in mechanical and electronic properties introduced by the interfacial regions of SEs.

From a comprehensive library of 590 surface and GB models of SEs, we conclude that the energy to mechanically "separate" GBs can be significantly lower than their bulk analogs, which can trigger preferential cracking of SE particles at their GB regions. Compared to the respective bulks, the excess volumes of GBs arise from the different coordination environments experienced by the chemical species expressed in these defects. From our models, we observed that GBs and surfaces of SEs will introduce new electronic "interfacial" states within SE gaps. These interfacial states alter and possibly increase the availability of free electrons and holes in SEs. An imbalance of holes and electrons near these extended defects can potentially increase the local electronic conductivity of SEs and thus facilitate failure-inducing metal plating.

2. Results

To establish a comprehensive overview of the effect of extended defects in SEs, we investigate representative electrolyte chemistries. We investigate the orthorhombic γ-Li_3PO_4,[43] and its thiophosphate analog β-Li_3PS_4.[44] For a comparison between Li and Na thiophosphates, we considered Na_3PS_4 (both the cubic and the tetragonal phases).[45–49] We included the argyrodite Li_6PS_5Cl as an example of halogenated thiophosphate SEs.[50–53] Among the oxide ceramics, we included the garnet $Li_7La_3Zr_2O_{12}$ (LLZO).[37,54] We investigate the Natrium SuperIonic CONductor (NaSICON) with the composition $Na_3Zr_2Si_2PO_{12}$ as a representative mixed phosphate/silicate.[55–57] Prototypical halide SEs were described by Li_3YCl_6, which is claimed to be moisture-insensitive and stable against high-voltage positive electrode materials.[58–61] Binary compounds including Li_2S, Li_2O, Na_2S, and LiCl, whose reduced structural complexities enable a systematic exploration of their surfaces and GB models, were also included in this analysis. Moreover, these compounds are also commonly found as primary decomposition products of a broad range of oxide and sulfide SEs at specific potentials vs Li/Li^+ (or Na/Na^+).[6,50,62,63] The characteristics of SEs investigated in this work are listed in Table S1, Supporting Information.

2.1. Construction of Surfaces and Grain Boundaries of Solid Electrolytes

Given the complexities associated with the study of extended defects,[26] such as GBs and surfaces of multi-component polycrystalline ceramic materials, the existing literature appears scarce, with this investigation aiming to close this knowledge gap.[30,38,42,64,65]

Starting from the experimentally reported bulk structures (organized in Table S1, Supporting Information), electrostatically sound slab models of distinct Miller indices surfaces were built.[27] All slab models are charge-neutral and symmetric and do not present intrinsic electrical dipole moments.[27,66] To downsize the vast set of possible SE surfaces, only a subset of surfaces up to Miller index = 3, or 2 for LLZO, NaSICON, and Li_3YCl_6

was explored. In polyanion systems, such as Li_3PS_4 and NaSICON, all the PS_4^{3-}, PO_4^{3-}, and SiO_4^{4-} moieties must be strictly preserved, which avoids alteration of the underlying chemistry of these SEs.[67] To balance the charge after preserving the integrity of polyanion moieties, such as PO_4^{3-} or SiO_4^{4-}, some surface atoms (Li, Na, O, or S) have to be removed, thus introducing off-stoichiometry in SEs' models. This criterion also ensures that only weak Li(Na)–S or –O bonds are broken, leading typically to low surface energy models.[34,68] For each Miller index, several distinct surfaces—that is, chemically different terminations—can exist. For example, in LLZO, surface cuts along specific Miller planes may differ among the exposed species, O, La, Li, and Zr, with different stabilities (reactivities).[69]

While implementing these strategies downsizes the total number of surface cuts, still 10^5 distinct surface models may still be found. To circumvent this limitation, only representative surface models carrying the lowest classical Ewald energy were selected for subsequent GB construction.[70,71] As surfaces of SEs are the starting block to build GB models, Figures S3, S4, and S5, Supporting Information, show the predicted crystal morphologies of each SEs, in terms of their Wulff shapes.

In polycrystalline SEs, several types of GBs can be envisioned, such as, tilting, twinning, etc., which are formed from the interface of multiple chemically terminated grains of SEs. Hence, to reduce the types of GBs, we have considered twinning types of a selection of chemically meaningful terminations of SEs,[72] including non-stoichiometric cases. It has been shown that low-index twinning GBs tend to possess low energy,[73] for example, Σ3(111) in Li_3ClO[74] (0.34 J m^{-2}) or Σ2(110) in $Li_{0.16}La_{0.62}TiO_3$[75] (0.30 J m^{-2}). Experimentally, twin boundaries have been observed in various perovskite samples, including $BaTiO_3$, $SrTiO_3$, $BaZrO_3$, and $CaMnO_3$.[76–78]

Twinning-type GBs are formed by placing together one slab model of a selected Miller index (representing the bottom grain) and its mirror image along the cutting plane (as the top grain), with the exposed surfaces of the two grains in parallel. The degrees of freedom explored in these GBs are discussed in Section S2, Supporting Information. Therefore, the top grain is rotated by an angle of 180 ° to the bottom grain. This rotation introduces a misorientation between grains. In this paper, Miller indices of surfaces and the twin GBs are indicated as (h, k, l) and $\{h, k, l\}$, respectively. To reduce the number of degrees of freedom arising from the rigid translations between two grains (slabs), we searched the "global" minimum of the potential energy surface—the Σ-surface,[79] which is the energy hyperplane formed by the in-plane rigid translations of each grain (slab) of the GB model. Details are discussed in Section S3, Supporting Information.

2.2. Mechanical Properties of Grain Boundaries

Quantifying the mechanical properties of SEs, in particular, those of air-sensitive materials, represents a major experimental endeavor.[42] Important thermodynamic quantities qualifying the surfaces and GBs include: i) The surface energy, γ, of Equation (3) is the energy to cut out a surface from the bulk SE. ii) The GB excess energy, σ, of Equation (5) is the excess energy of GB per unit area compared with the bulk. iii) The work of adhesion, W_{ad}, of Equation (7) which is the energy absorbed per unit area when separating a GB into two surfaces. iv) The cleavage energy, W_f, of Equation (4) is the energy absorbed per unit area to separate the bulk into two surfaces. W_f is twice the surface energy, γ of the stochiometric surface with the lowest γ (i.e., the most stable surface cut). v) The GB formation energy, E_f, of Equation (6) is the excess energy of GB per atom compared with the bulk. Thus, E_f quantifies the thermodynamic stability of a GB model.

Figure 1 shows the general trend of computed work of adhesion (W_{ad}, in Equation (7)) of several GBs in Li_2O, LiCl, Li_2S, Na_2S, Li_3PO_4, Li_3PS_4, Na_3PS_4, Li_3YCl_6, Li_6PS_5Cl, $Li_7La_3Zr_2O_{12}$, and $Na_3Zr_2Si_2PO_{12}$. The width of each sector is proportional to the Boltzmann distribution of the formation energy, which provides a visual measure of the thermodynamic abundance of specific GBs.

The radius of each sector is the work of adhesion, W_{ad}. Figure 1 reports only the GBs with the lowest values of σ.

Evaluating the distribution of works of adhesion, W_{ad}s, for several SEs and comparing these values with their W_fs gives insights into the mechanical stability of the SEs' GBs. It was proposed that the population of GB is inversely proportional to the value of excess energy, σ.[78,80,81] GB models of each SE chemistry are sorted by a Boltzmann probability distribution $p(N, V, T) \propto e^{\frac{-E_f}{kT}}$ of the GBs' formation energies E_f, with k the Boltzmann constant, E_f the formation energy defined in Equation (6), and T the reported synthesis temperature of each SEs (see Section S5, Supporting Information). For Li_2S, LiCl, Li_2O, and Na_2S, we set $T = 273$ K.

In general, the range of computed work of adhesion, W_{ad} of Figure 1 appears very broad. For example, in Li_2S, the work of adhesion, W_{ad} can be as low as 28% (≈0.2 J m^{-2}) of its W_f (≈0.7 J m^{-2}). The surface energies γ of oxide SEs are generally larger than 0.5 J m^{-2}, whereas, for sulfides and chlorides, both the GB excess energy, σ, and the surface energy, γ are generally smaller than 0.5 J m^{-2}. γ and σ are related in Figure S6, Supporting Information.

It is important to analyze trends in the GB work of adhesion, W_{ad} for simple Li binary systems, that is, Li_2O, Li_2S, and LiCl. By comparing the cleavage energy, W_f, and the work of adhesion, W_{ad} of each Miller index of the Li_2O, Li_2S, and LiCl, their mechanical stabilities follow the order $Li_2O > Li_2S >$ LiCl. The values of the work of adhesion, W_{ad} in Figure 1 suggest that ternary compounds, such as Li_3PO_4, Li_3PS_4, and Na_3PS_4 are weaker than binary compounds (Li_2O, Li_2S, and Na_2S). This trend is explained by the inductive effects of the polyanionic moieties that weaken the Li(Na)–O(S) bonds.[82–84] In Figure 1, Li_3PO_4 (0.9 J m^{-2}) has about twice the value of cleavage energy, W_f of Li_3PS_4 and Na_3PS_4 (both ≈0.4 J m^{-2}). The comparison of Na_3PS_4 with Li_3PS_4 is less immediate, as these two SEs have different crystalline structures.[43,44] Previous work suggested a high similarity between the cubic and tetragonal phases of Na_3PS_4,[83] which explains the similarities in the work of adhesion, W_{ad} of these polymorphs.

The construction of GB models of $Li_7La_3Zr_2O_{12}$ (LLZO) requires breaking the interconnected oxide frameworks, which may lead to relatively high surface energies, γs (at least ≈0.9 J m^{-2} for stochiometric cases), and therefore, LLZO shows the largest value of cleavage energy, W_f (1.8 J m^{-2}) among all SEs investigated here. As a comparison, in Li_3PO_4 the PO_4^{3-} tetrahedra do not share corners/edges, therefore the energy for breaking the

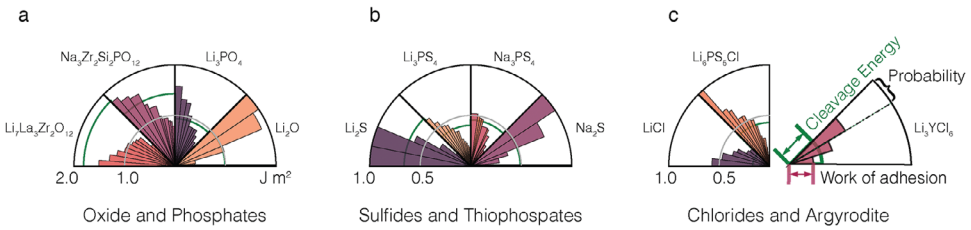

Figure 1. Predicted work of adhesion, W_{ad} of various SEs' grain boundaries. $Li_7La_3Zr_2O_{12}$ (LLZO), and $Na_3Zr_2Si_2PO_{12}$ (NaSICON). The radial length of each sector is the W_{ad} (Equation (7)) of each GB. The width of each sector is proportional to the relative thermodynamic abundance of each GB evaluated from a Boltzmann distribution of the formation energy (Equation (6)) of all GBs of each SE. Each GB model may show different chemical terminations and different σ; here, models with the lowest value of σ (see Equation (5)) are reported. Green lines are the fracture (cleavage) energies of SEs in J m^{-2}. The maximum scales of W_{ad} and W_f are: 2.0 J m^{-2} for oxides/phosphates, 1.0 J m^{-2} for sulfides/thiophosphates, LiCl, and argyrodite, and 0.5 J m^{-2} for Li_3YCl_6. The data graphed in this figure is tabulated in Section S6, Supporting Information.

Li–PO_4^{3-} bonds appears low (the lowest $\gamma \approx 0.5$ J m^{-2}). Looking more closely at LLZO, the estimated excess energies σ range between 0.6 and 1.4 J m^{-2}.[64] Off-stoichiometric surfaces and GBs are expected to dominate the LLZO grains.[69,85] A nonstoichiometric GB of LLZO $\{11\bar{1}\}$ (i.e., $28Li_7La_3Zr_2O_{12} + 2La_2O_3 + 14Li_2O$) with excess O, La, and Li displays the lowest excess energy, σ (0.6 J m^{-2}). Unsurprisingly, a stochiometric Zr-terminated {001} GB of LLZO has the largest σ (1.4 J m^{-2}). This implies that Li-rich GBs and surfaces[69] may be preferred and act as a natural Li-ion reservoir. The values of the work of adhesion, W_{ad}s, are similar for the Li or La terminated surfaces (0.8–1.2 J m^{-2}), but remain significantly lower than for the Zr terminated surfaces (1.5–1.7 J m^{-2}) in LLZO.

Similar to LLZO, $Na_3Zr_2Si_2PO_{12}$ (NaSICON) displays a 3D rigid framework. The construction of NaSICON surfaces also involves cutting Zr–O bonds, which leads to high surface energies, γs ranging from 0.9 to 1.5 J m^{-2}. These surfaces are generally terminated by sodium and oxygen atoms, the latter taking part in PO_4^{3-} and SiO_4^{4-} moieties. There is no significant difference in the work of adhesion, W_{ad} (ranging between 0.9 and 1.8 J m^{-2}) between stoichiometric and nonstoichiometric GB models in NaSICON, while σ of the nonstoichiometric grain boundary (0.9–1.5 J m^{-2}) is generally larger than the stoichiometric GBs (0.1–0.5 J m^{-2}).

Compared with other SEs of Figure 1, Li_3YCl_6 shows low values of work of adhesion, W_{ad} and cleavage energy, W_f (≈0.13 J m^{-2}). This indicates the softer nature of Li_3YCl_6 and chloride materials, as well as their low mechanical stability. This finding is further confirmed by the ease of forming stacking faults in Li_3YCl_6 and similar halide SEs.[61] By inspecting the most stable surface cuts of Li_3YCl_6, we observed that the YCl_6^{3-} moieties are preserved at the expense of easier-to-cleave Li–Cl bonds.

The argyrodite Li_6PS_5Cl can be expressed as a 1:1:1 mixture of Li_2S, LiCl, and Li_3PS_4. In Li_6PS_5Cl GBs and surfaces show either PS_4^{3-} moieties or dangling Li–Cl and Li–S bonds. Remarkably, the surface energies of Argyrodite SEs sit in between that of Li_2S, LiCl, and Li_3PS_4 in agreement with ref. [86]. Synthesis conditions and working conditions of Li_6PS_5Cl will set S-rich or S-poor environments, which are tuned by the sulfur chemical potential S (derived from our phase diagrams in Section S8, Supporting Information).[53] Unsurprisingly, in an S-rich environment, the excess energy, σ of nonstoichiometric S-rich GBs is significantly lower compared with S-poor environments. For example, σ of a nonstochiometric $\{11\bar{1}\}$ GB in an S-rich condition is ≈0.23 J m^{-2} in an S-rich environment, and ≈0.57 J m^{-2} in an S-poor environment. From Equation (5), the synthesis conditions of these SEs control the excess energy of GBs and therefore also the population of GBs, as the excess energy, σ appears linearly proportional to E_f, whereas E_f is inversely related to the GBs' Boltzmann population. This implies that in S–rich synthesis conditions, S-rich GBs are formed. We also found that the S-rich GBs have higher work of adhesion, W_{ad} compared with S–poor grain boundaries, possibly due to segregated Li_2S being "stronger" than LiCl in S–poor GBs. This observation suggests that the mechanical stability of argyrodite particles can be controlled by appropriate synthesis conditions, and the mechanical stability of GB can be achieved with excess sulfur in the synthesis environment.[53]

2.3. Volume Changes in Grain Boundaries of Solid Electrolytes

During the formation of GBs from the bulk, volume changes are introduced in the GB regions to accommodate the different coordination environments of atoms. These volume changes are referred to as GB excess free volumes (BFVs) per area.

$$\Omega = \frac{1}{2S} \times \left[V_{GB} - 2N_{slab} V_{bulk}\right] \quad (1)$$

where V_{GB} is the volume of the GB model of SE and V_{bulk} is the volume per formula unit of the bulk structure of SE. Ω can be understood as the absolute values of how much the normal axis to the GB plane varies in the GB region compared to the reference bulk lattice.[87] **Figure 2** shows the relationship between the GB excess energy, σ, and the excess volume, Ω of GB models. Overall, it appears that the GBs with large excess volumes tend to have high excess energy. It is important to understand the connection between the excess volume, Ω, and the excess energy, σ of GBs. Densifications through spark-plasma sintering imply pressure in the order of GPa's. Assuming 1 Gpa of applied pressure to a polycrystalline SE carrying an excess volume of ≈1.0 Å, an additional excess energy on the GB compared with the bulk can be estimated as 1.0 GPa × 1.0 Å = 0.1 J m^{-2}. This implies that the GBs with high excess volume can be suppressed due to additional excess energy induced by pressure, which is consistent with the effect of densification, that is, sintering. In Figure 2, Li_3PS_4 and Na_3PS_4 feature GBs with high-excess volumes. Under 1.0 GPa of applied pressure, their excess energies would be nearly

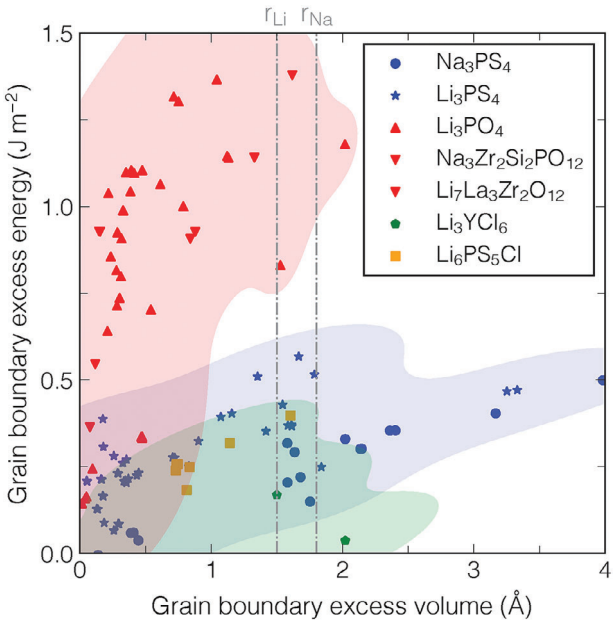

Figure 2. Relationship between the excess volume Ω (in Å) and excess energy σ (in J m^{-2}) of GB models of different SEs. Each data point corresponds to a GB model. Gray lines mark the atomic radii of Li and Na. Colors categorize GBs that share "similar" chemistries.

doubled, hence the substantial effects that hot-pressing can impart on these thiophosphates.

2.4. Electronic Structure of Extended Defects

Structural changes introduced by the presence of extended defects are the results of the combination of chemical processes where existing bonds are broken and new bonds are formed. These chemical processes will unavoidably alter the underlying electronic structure (the band structure) of GBs and the surfaces of SEs compared to their bulks.

Figure 3 emphasizes changes in the "local" bandgap of several SEs caused by extended defects, such as surfaces and GBs. In general, compared to GB models, the surfaces of SEs show a greater decrease in bandgaps from the respective bulk structures. Cleavage of surfaces of SEs implies breaking selected bonds and a subsequent reduction of species' coordination number, which explains the large extent of reduction of bandgap compared to SEs due to surface states.

Variation of electronic structure properties is particularly accentuated in oxide-based SEs. A bandgap decrease can be as high as ≈3.0 eV in the case of Li_3PO_4 and Li_2O surfaces, which implies that the breakage of Li–O bonds is similar to breaking the Li–PO_4 bonds. For LLZO, the formation of extended defects involves breaking Li–O, La–O, and Zr–O bonds, with bandgap changes in GB models as high as 1.3 eV, whereas the bandgap change can go up to ≈3.7 eV in the (001) Zr-terminated surface. We recalculated the band structure of this surface model by HSE06 hybrid functional and the bandgap was only 1.8 eV. Changes in bandgap appear somewhat smaller in NaSICON GBs and surfaces (up to 2.2 eV) compared to a pure complex oxide, such as LLZO.

The electronic structures of sulfides and thiophosphate materials appear less sensitive to the introduction of GB and surface defects compared to oxides and phosphates. The largest bandgap decrease of ≈1.0 eV about their bulks is reported for GBs and surfaces of Li_2S, Na_2S, and Li_3PS_4. Many surface models display bandgap changes from their bulk references that are close to 0 eV. This is the case on the Li_2S (210), the Na_2S (111), and the Li_3PS_4 (001) surfaces. The same observation can be extended to Na_3PS_4, where there is almost no bandgap change upon the formation of surfaces and GBs. Chloride SEs show a moderate change (up to 2.5 eV from the bulk reference) in the bandgap. Unsurprisingly, the bandgap drop of surfaces and GBs of argyrodites lie between LiCl and Li_3PS_4.

A closer inspection through a comparison of the electronic structures of bulk and GBs or surfaces of SEs reveals that extended defects introduce additional states in the bulk bandgap region rather than merely moving closer valence and conduction bands. The position of new energy levels—the interfacial states—introduced by extended defects in the bandgap of bulk SEs does affect the electronic conductivity of the material if these levels are sufficiently close to the band edges, that is, the valence band maximum (VBM) and conduction band minimum (CBM). In contrast, deep defect levels that appear farther away from the band edges will form localized states that will negligibly affect the electronic conductivity of SEs.

To quantify the extent of localization of defects introduced by GBs and surfaces, the inversed participation ratio (IPR) is used.[88] The IPR is defined as $\frac{N\sum_{i=1}^{N}[p_i]^2}{(\sum_{i=1}^{N}[p_i])^2}$, where p_i is the electron density at site i, and N the total number of sites (atoms). For completely localized states IPR = 1.0, whereas for evenly unlocalized states IPR = $\frac{1}{N}$. For example, Section S9, Supporting Information, compares the density of states and IPR plots of bulk LLZO with those of the Zr-terminated (001) surface, and the corresponding GB. In contrast, the conduction band and valence band of the bulk structure are dense and continuous (Figure S8, Supporting Information), and interfacial states introduced by the surface (Figure S9, Supporting Information) and GB (Figure S10, Supporting Information) are sharp and isolated in the bandgaps. Such states are generally localized, as inferred by the high values of IPR. Due to the larger density of broken bonds in surface models, more interfacial states are introduced in the gap compared to GBs. However, localized states may not contribute to electronic conductivity, but may promote local polarizations if localized states are near the surfaces of SEs.

As shown in Figure S11, Supporting Information, GBs with high values of σ, which are less thermodynamically stable, tend to show larger variations in their bandgaps compared to their reference bulks. Unstable GBs exhibit extended structural reconstruction due to the higher densities of broken bonds and significantly reduced coordination environments (of specific atoms) compared to their bulk counterparts. This leads to a notable alteration in the electronic structures of these GBs.

2.5. Stability of Solid Electrolytes Surfaces to Metal Anodes

Through a procedure of band alignment, we explored the electronic collocation of different SE surfaces to those of Li and Na metals. The work function of Li ($-E_{Fermi}$ in **Figure 4**) lies in the

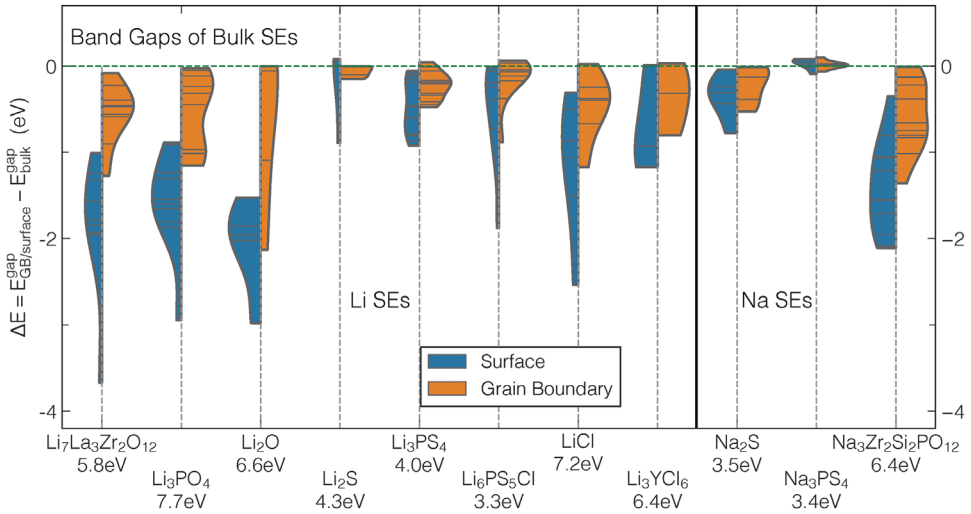

Figure 3. Variation in predicted bandgaps (in eV) in GB and surface models of SEs compared to their bulk analogs. Orange shapes show the distribution in bandgap change of grain GBs to their bulks, while the blue shapes are for surface (slab) models. Each horizontal line of violin shapes represents the most stable GBs (or surfaces) models of various crystallographic directions, and thus violin shapes with large widths indicate stable GBs or surfaces with high probability. The horizontal dashed line sets the bulk reference. The bandgap change is calculated based on the semi-local GGA (PBE) bandgap of each SE. Accurate hybrid functional bandgaps (HSE06) of bulk SEs are reported as a reference under the respective chemical formulas of SEs.

range of 2.7 to 3.2 eV, which is in good agreement with previous experimental work.[89] The work function for Na ranges from 2.5 to 2.9 eV.

In Figure 4 tops of the bottom bars and bottoms of the top bars are the band edges, that is, the VBM and the CBM of each surface model of the SE. In practice, the CBMs represent the electron affinities of the surface models of each SE, whereas the VBMs represent the ionization energies. An overlap of the conduction band in SEs with the Fermi energies of metal electrodes is a signature of the chemical reactivity of these materials.

Unsurprisingly, binary compounds, such as Li_2O, Li_2S, Na_2S, and LiCl show electron affinity values far apart from the potentials (Fermi energies) of Li (or Na), which confirms the intrinsic stability of these binary compounds when in contact with metal electrodes. Thiophosphates,[62,90,91] chlorides,[92,93] and as a mixture of chloride, thiophosphate, and sulfide, argyrodites are likely to be reduced by metallic Li.[10,62,92,94,95] Furthermore, the electron affinity of different SEs varies as a function of the Miller index. In Li_3PS_4 the (112) surface has the largest large electron affinity (≈3.4 eV), which makes it prone to react with Li metal, whereas the (011) surface with an electron affinity ≈2.1 eV seems to be stable against Li metal.

Despite the large bandgap drop of oxide-based SEs, the electron affinities of oxides are smaller than the work function of the corresponding metal (Li or Na).[91] Although Li_3PO_4 appears stable against the Li-metal anode,[96] NaSICON is

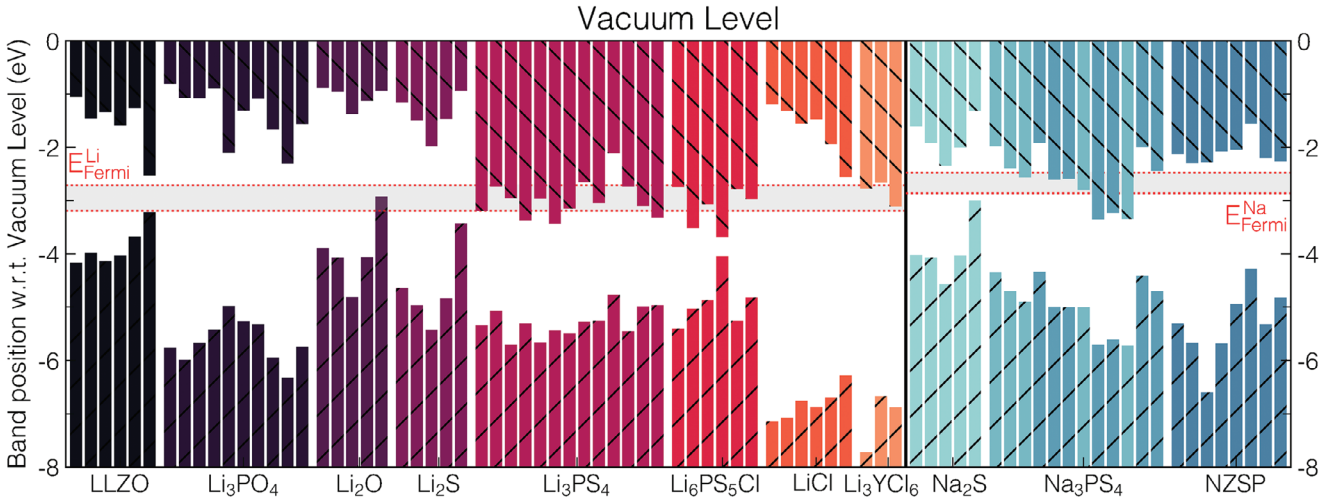

Figure 4. Alignment of SE surfaces versus Li and Na metal references indicated by the gray areas enclosed in red dotted borders. The *y*-axis is the energy level relative to the vacuum level of each SE, with $y = 0$ indicating the vacuum level. The upper bars are the conduction band minima, and the bottom bars are the valence band maxima of each SE. NZSP refers to NaSICON $Na_3Zr_2Si_2PO_{12}$.

thermodynamically unstable against Na metal,[97,98] which Figure 4 does not correctly capture. Indeed, the surface terminations appear to play an important role in these systems. Although we observed a large bandgap drop in a Zr-terminated (001) surface, the conduction band of LLZO still lies slightly above the Li metal Fermi energy, which agrees with previous results.[85]

3. Discussion

Using a thermodynamic model established through accurate first-principles calculations of several topical oxide, sulfide, and halide SEs, we reveal the effects introduced by extended defects, such as grain boundaries (GBs) and surfaces, on the thermodynamic, mechanical, and electronic properties of polycrystalline SEs.

The work of adhesion, W_{ad} was identified as a major descriptor for the mechanical strength of polycrystalline SEs, and thus the characterization of their GBs. The work of adhesion, W_{ad}, and other mechanical properties consolidated here provides an accurate set of parameters for the parametrization of continuum models to describe SEs. Irrespective of the type of chemistry, ternary lithium (and sodium) phosphates, thiophosphates, and chlorides show inferior mechanical properties than their respective binary compounds (Li_2O, Li_2S, and LiCl).

SEs displaying rigid frameworks, such as LLZO and NaSICONs provide larger values of work of adhesion, W_{ad}, and cleavage energy, W_f, than phosphates, thiophosphates, or chlorides. In LLZO GBs, values of work of adhesion, W_{ad}, are systematically larger than sulfides and chloride SEs in Figure 1, but smaller than Li_2O, Li_3PO_4, and NaSICON. This is due to the high-grain boundary excess energy of LLZO, considering its negative contribution to the work of adhesion, W_{ad} (as defined in Equation (7)).

At the low potential set by Li-metal, Li_2S, and Li_3P are common decomposition products of sulfide SEs (e.g., Li_3PS_4).[62,63,99] These binary compounds display values of cleavage energies, W_f (≈0.7 J m^{-2} for Li_2S, and 1.0 J m^{-2} for Li_3P) higher than Li_3PS_4 (≈0.4 J m^{-2}).[99] Although it is tempting to claim an increase in fracture toughness of the "composites" formed by a SE and its decomposition products, due to the higher toughness of the latter compared to the SE alone, this is probably incorrect as "the fracture toughness of the composite" will depend on the weakest link, among the fracture toughness of the SEs (cleavage energy and GB work of adhesion) and the delamination of binary interfaces (works of adhesion of the composite-interface). Understanding the interplay of these forces remains an extremely complicated task, which requires a complete understanding of the microstructures, particle size distributions, morphologies, and porosities of such complex composites.

The relative strength of GBs versus bulk of a SE may drive the type of fracture pattern as either intergranular fracture—it occurs in the grain boundary—or as transgranular——occurring in the grain. The fracture energy ratio $R_{\rho p}$ between the work of adhesion W_{ad} and the cleavage energy W_f is often used as a descriptor to discriminate the type of fracture pattern in ceramics.[100–103] A simulation study on Al_2O_3 suggested that intergranular fracture is preferred when $R_{\rho p} < 0.5$.[100] In addition, the fracture mechanism also depends on the portion and distribution of GBs in the materials,[101] the temperature, the strain rate,[104] and the grain sizes.[105] Furthermore, the "wettability" of the SE by the metal anode, namely, the interfacial energy between the anode metal and the SE, may affect the behavior of the fracture. It is also possible that the active metal (Li or Na) penetrates the SEs simultaneously as the crack propagates, which is different from the current assumption of this work envisaging the propagation of the crack front before the metal ingress.[33] In this mechanism, instead of introducing voids between cracked grains, new interfaces between metal and SE are formed. The energy change of this process can be measured as the interfacial formation energy between the SE and the metal,[99] instead of W_{ad} and W_f here. However, strained epitaxial interfaces remain ambiguously defined and probably very unlikely in a polycrystalline material.

Here, the simulated thermodynamic properties of these SEs are integrated with elements of fracture mechanics. The fracture toughness, K_{Ic} under crack opening, illustrative of brittle ceramics, is defined in Equation (2).[106,107]

$$K_{Ic} = \frac{\sqrt{E\,G_c}}{\sqrt{(1-\nu^2)}} \tag{2}$$

where for a SE, E is its Young modulus, ν is its Poisson ratio, and G_c is the critical energy release rate required for crack propagation. In most derivations of Equation (2), $\sqrt{(1-\nu^2)}$ is omitted, as this value typically approaches unity.[106] Considering LLZO a hard brittle ceramic,[108] we approximate G_c by the computed cleavage energy, W_f of ≈1.8 J m^{-2},[106] an approach that appears accurate to investigate materials in their linear-elastic regime. Here, using Young's modulus of 163 GPa and a Poisson ratio of 0.26,[8,109,110] a fracture toughness of ≈ 0.56 MPa · $\sqrt{\text{m}}$ is derived. Our computed value (≈ 0.56 MPa $\sqrt{\text{m}}$) appears to be in excellent agreement with previous experimental results of 0.60 MPa $\sqrt{\text{m}}$.[111] Notably, the experimental values of K_{Ic} for LLZO demonstrate a wide distribution, ranging from 0.44 to 1.63 MPa $\sqrt{\text{m}}$.[8,110–114] Therefore, thermodynamically stable GB (twin-type) set a lower bound on the spread of expected fracture toughness, K_{Ic}.

Several factors may contribute to the spread of values of K_{Ic}, for example: the occurrence of dislocations in regimes of plastic deformation;[115] the anisotropic behavior of polycrystalline specimens;[107] different experimental measurements (e.g., nanoindentation vs microindentation); sample conditions, including grain size, porosity, and the availability of impurities; and the singularity at the crack field.[107,115] For the reasons discussed above, it remains difficult to reproduce experimentally measured values of some SEs.

From this analysis, it emerges that the mechanical strength of SEs can be improved through their amorphization or by doping. Amorphization of materials reduces the density of GBs, and may be beneficial to improve the overall mechanical strength of SEs. It has been discussed that the amorphous sulfide SEs possess higher formability than their crystalline counterparts due to the isotropic nature of amorphous solids and their larger molar volume per atom.[116,117] Recently, the group of Rupp has extended amorphization procedures to hard oxides, in particular, LLZO.[118]

From our simulations and previous experiments, it has been observed that Li-ions (and Na-ions) tend to aggregate near the facets (surfaces) of SE particles. The bond strength imparted

by Li/Na-ions in between two grains is minimal because of the high mobility (low bonding strength) of these ions. In addition, the most stable coordination environment of Li-ion is four, hence minimizing the number of bonds with surrounding anion species. Therefore, adding non-redox active multivalent dopants with a preferred coordination number larger than 4 and/or a higher bond strength with cation can strengthen the texture of the grain boundary by increasing the bonding between grains.

However, as cycling stresses are applied to polycrystalline SEs during repeated charging/discharging,[42,119] the density of accumulated dislocations arising from plastic deformation of SEs (and electrodes) may contribute to the degradation of SEs, and even induce fractures.[42] From this perspective, linear-elastic measures of cleavage energy, W_f and work of adhesion, W_{ad} can be a conservative, but safe approximation to evaluate the strength of solid-state electrolytes instead of G_c. In particular, a recent experimental investigation of Li penetration in LLZO demonstrated that the observed stress field of the SE shows an elastic (linear) behavior, and is thus in agreement with our approximation of cleavage energy, W_f of Equation (2).[120] If G_c is taken as a measure of mechanical stability, Jokl et al.[121] proposed that G_c is a monotonic function of the cleavage energy, W_f. This suggests that GBs with work of adhesion, W_{ad} smaller than their bulk cleavage energies should show smaller values of the critical energy release rate. Meanwhile, Young's moduli of SEs are expected to decrease near GBs' regions.[65,122,123] For example, Yu et al. [109] demonstrated that in the Σ5 GB of LLZO, the moduli (including the Young modulus) can decrease as much as 50% (from that of bulk), which leads to smaller values of the fracture toughness of this SE. This implies that GBs in SEs are an obvious source of crack initiation, as GBs are prone to fracture from the induced stresses of penetrating Li, perhaps as Li filaments during specific electrochemical conditions.

Although using the computed cleavage energy, W_f to approximate the G_c tends to underestimate measured values of the K_{Ic} fracture toughness of SEs, it is still informative to extend the estimation of K_{Ic} to all the SE materials investigated in this work. **Figure 5** summarizes the estimated fracture toughness of the bulk region and GB region. Solid bars in Figure 5 show an estimated lower limit of fracture toughness using the weakest GB model (see Figure 1) of each SE, where the critical energy release rates, G_cs of Equation (2) are estimated by the minimum value of work of adhesion, W_{ad} while assuming a 50% reduction of the SE Young's modulus.[109] The translucent bars in Figure 5 are estimated upper limits of the fracture toughness of the bulk SEs, where G_c is estimated by the cleavage energy, W_f of bulk SE.

In Figure 5 computed values of fracture toughness K_{Ic}s of oxides-like SEs are systematically larger than sulfides and chlorides. Therefore, our model correctly captured the general trend of fracture toughness of SEs, with oxides ≫ sulfides > chlorides. Unsurprisingly, LLZO displays the highest fracture toughness for both GBs (solid bar) and bulk (translucent bar), due to the high cleavage energy W_f, work of adhesion W_{ad}, and Young's modulus. Argyrodite Li_6PS_5Cl possesses the smallest fracture toughness of GBs, while Li_3YCl_6 shows the smallest bulk fracture toughness among all SEs considered. In general, the fracture toughness of bulks is approximately twice that of GBs.[42] An anomaly to this trend is LiCl as it is difficult to identify GB models with work of adhesion, W_{ad} smaller than the cleavage energy, W_f.

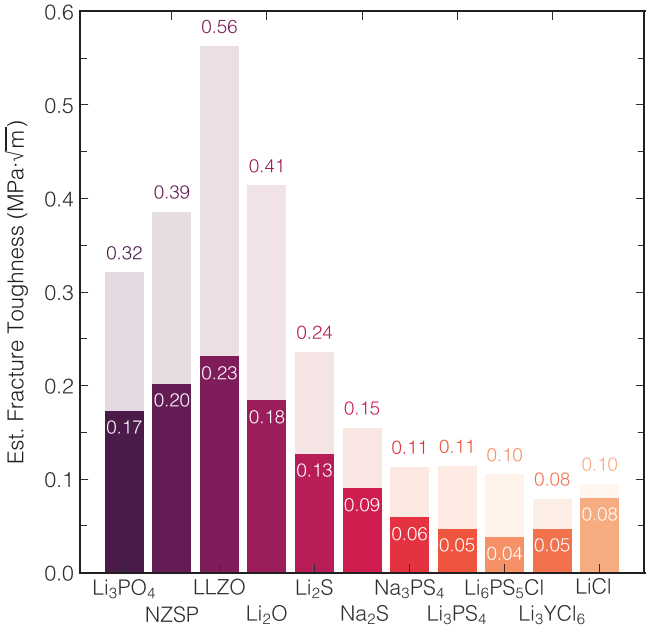

Figure 5. Estimated fracture toughness K_{Ic}s from Equation (2) of SEs derived from computed cleavage energy, W_f and work of adhesion, W_{ad}, respectively. LLZO is for $Li_7La_3Zr_2O_{12}$, and NZSP is for $Na_3Zr_2Si_2PO_{12}$. Details used in calculations of Figure 5 are in Table S4, Supporting Information.

Recently, Ning et al.[30] claimed that the initiation of a Li(Na) deposition can be linked to the fracture toughness of GBs in SEs, and proposed a numerical model to directly evaluate the critical current density before Li can start depositing. Upon evaluation of the *J*-integral associated with SEs' fracture under external stress, for example, that of inserting Li, it was hypothesized that larger values of fracture toughness lead to higher critical Li current densities. This highlights the importance of GB's fracture strength instead of macroscopic fracture toughness and emphasizes the importance of GB engineering for SE synthesis.

The fracture stress, that is, the critical tensile stress for crack propagation of a material, can be calculated by $\zeta_c = \frac{K_{Ic}}{\sqrt{Ya}}$,[124] where K_{Ic} is the fracture toughness, Y is the shape factor, and a is the flaw size. The stress required for crack propagation will be small at the GB region compared to the bulk region. This investigation provides the simulation data for the fracture toughness, which can be directly linked to the fracture when a flaw size is hypothesized. Several studies suggest that pure Li metal with a diameter of 76 nm can support up to 244 MPa under uniaxial compression. This raises new challenges for designing more ductile, fracture-resistant SEs.[42,125] Ning et al.[33] claimed that metal filaments can open the crack and penetrate through Li_6PS_5Cl SE. In light of this experimental observation, it can be expected that SEs whose GBs are weaker than that of Li_6PS_5Cl will be less resistant to the stress imparted by Li-metal filaments. From our analysis, chloride SEs, such as Li_3YCl_6, are expected to show poor electromechanical resistance toward Li-metal ingress.

In contrast to oxide SEs (LLZO, NaSICON, and Li_3PO_4), the large excess volume estimated (see Figure 2) in sulfide and chloride SEs implies an abundance of free space for interstitial atoms, which results in low segregation energy,[126] especially of

small atoms such as Li ions. [127] Speculatively, the large excess volumes observed for halide and thiophosphate SEs might be the reason that their GBs do not largely affect the ionic conductivity of these SEs. However, the large excess volume may also facilitate metal deposition.

It was proposed that the GB excess energy is controlled by their elastic energy, which can be estimated as the product of the SE shear modules, the excess volume, and the energy contribution arising from atomic bonding.[128] The GB elastic energy arising from excess volume can be estimated via $\gamma_s = \frac{2}{3}\Omega G$, where the γ_s is the GB elastic energy and G is the shear modulus. Except for the linear behavior of LiCl and Na_3PS_4, most SEs do not follow a linear relationship between the excess energy σ and Ω (Figure 2). However, even in LiCl and Na_3PS_4, the elastic energy appears twice (and even three times) larger than the excess energy σ. The lack of any linear relationship between γ_s and G has been previously discussed in ref. [129]; the authors suggested that the excess volume is not a reliable indicator of the excess energy, especially in hard-ceramic systems with as many SEs (Figure 5).

Knowledge of relevant thermodynamically sound GB models of SEs and their surfaces is extremely useful for investigating the variation of electronic properties introduced by these types of extended defects. Figure 3 summarizes the bandgap change of surfaces and GBs of SE we studied, as an indicator of change in electronic structure. The formation of surfaces and GBs of SEs causes the removal and formation of new bonds, resulting in the introduction of "interfacial states" in these materials.[50] In practice, these interfacial states may trap excess electrons,[35] and can cause a sudden reduction of SE's bandgaps. Changes in bandgaps can have an immediate impact on the electronic conductivity of SEs.[50] For example, a recent investigation via advanced transmission electron microscopy detected a sudden decrease of the bandgap in the GB region of LLZO, which was linked to a potential cause for Li filament growth.[41]

4. Conclusion

The functional properties of polycrystalline materials, including solid electrolytes, are modulated by surfaces and grain boundaries occurring between grains. Through a unified methodology relying on first-principles calculations, an extensive library of thermodynamic and electronic properties of surfaces and grain boundaries of solid electrolytes for a total of 590 models. Structure-property relationships between extended defects, such as surfaces and grain boundaries of solid electrolytes, and their mechanical and electronic properties are established.

Twinning-type grain boundaries show low excess energy, indicating that they are representative of grain boundaries in polycrystalline SE materials. The low work of adhesion of grain boundaries compared to the cleavage energy of bulk indicates that grain boundaries can be the source of crack initiation in polycrystalline solid electrolytes. The brittleness of many oxide solid electrolytes, such as $Li_7La_3Zr_2O_{12}$ and $Na_3Zr_2Si_2PO_{12}$ contributes to their cracking under local pressure exerted by Li/Na ingress in their grain boundaries. Therefore, strategies of grain boundary engineering, doping, or amorphization of these solid electrolytes can help decrease the brittleness and increase the plasticity of these materials, and hence increase solid electrolytes' compliance to the exerted stresses caused by Li(Na)-metal penetration.

There is not a simple relationship between grain boundary energy and excess volume. Pressure optimization may be used to control the distribution of grain boundaries and their properties.

It is demonstrated that the occurrence of grain boundaries and surfaces alter significantly the electronic structure of solid electrolytes. The electronic properties of sulfur-containing solid electrolytes appear less sensitive than those of oxygen-based materials, which are much more prone to bandgap closure at grain boundaries. Both grain boundaries and surfaces introduce localized donor or acceptor states in the bandgap, which may contribute to local variations in electronic conductivities in solid electrolytes.

This analysis suggests that bulk properties alone are not sufficient for a complete assessment and engineering of solid electrolyte materials. Variations in mechanical and electronic properties at grain boundaries and exposed surfaces are of primary importance and should be addressed when evaluating new solid electrolytes and their devices.

5. Experimental Section

Energetics of Grain Boundaries and Surfaces: The excess energy of the surface (which was modeled as a slab) compared to the bulk was measured by the surface energy, γ of Equation (3).[27]

$$\gamma = \frac{1}{2S}\left[E_{slab} - N_{slab}E_{bulk} - \sum_{i}^{species} \Delta n_i \mu_i\right] \quad (3)$$

where N_{slab} is the number of formula units in the slab model, E_{slab} and E_{bulk} are approximated by the DFT total energy of the slab model and the bulk structure. S is the surface area of the model slab. For off-stochiometric slabs, such as argyrodite, LLZO, Li_3YCl_6, and NaSiCON, μ_i is the chemical potential of species i that is added (or removed) in quantity n_i in (from) the slab model. The values of μ_i were derived from the computed multidimensional phase diagrams of each SE. Details are discussed in Section S8, Supporting Information. Equation (4) defines the cleavage energy W_f, which is the energy required to crack the bulk SE and form two identical surfaces. In Equation (4), W_f amounts to twice the lowest surface energy, γ_{min} among all the stoichiometric surface cuts of a SE.[34]

$$W_f = 2\,\gamma_{min} \quad (4)$$

σ in Equation (5) defined the excess energy per unit area of a GB compared to its bulk,

$$\sigma = \frac{1}{2S}\left[E_{GB} - N_{GB}E_{bulk} - \sum_{i}^{species} \Delta n_i \mu_i\right] \quad (5)$$

where E_{GB} is the DFT energy of the grain boundary model, which contains twice as many formula units (f.u.) as the corresponding slab model. N_{GB} is the number of f.u. in the GB model, and S is the grain boundary area. For some off-stochiometric cases in argyrodite, LLZO, Li_3YCl_6, and NaSiCON materials, μ_i is the chemical potential of the species i, as defined in Equation (3). The formation energy of a GB, E_f is the GB excess energy per atom as defined in Equation (6).

$$E_f = \frac{1}{N_{atom}}\left[E_{GB} - N_{GB}E_{bulk} - \sum_{i}^{species} \Delta n_i \mu_i\right] = \sigma\,\frac{2S}{N_{atom}} \quad (6)$$

where N_{atom} is the number of atoms in the GB model. σ and E_f are connected, as shown in Equation (6).

From the quantities defined above, one defines the work of adhesion, W_{ad} of Equation (7) is the energy required to separate two grains to an infinite distance,[130] and quantifies the mechanical strength of a GB.[80]

$$W_{ad} = 2\gamma - \sigma = \frac{1}{2S}\left[2E_{slab} - E_{GB}\right] \quad (7)$$

First-Principles Calculations: Except for the calculations of the density of states, all the density functional theory (DFT) calculations were performed using the generalized gradient approximation[131] (GGA) for the exchange-correlation functional, as available in the Vienna ab initio Simulation Package version 6.3.0. A cutoff of 520 eV was applied for the plane wave expansion.[132] Core electrons were described by the projector-augmented wave method by Blöchl.[133,134] Dense Γ-centered, *k*-point grids ensured convergence of DFT calculations within 5 meV per atom. DFT total energies and interatomic forces converged within 10^{-5} eV and 0.01 eV $Å^{-1}$, respectively. In all the bulk, surface, and GB models, the atomic positions were fully relaxed with the approximations stated above. In GB models, the *z* (non-periodic) direction of the model was relaxed, while for slab models, all the lattice parameters were fixed to their respective bulk values. A vacuum of at least 15 Å was employed in the surface models.

Supporting Information

Supporting Information is available from the Wiley Online Library or from the author.

Acknowledgements

The authors acknowledge funding from the National Research Foundation under NRF Fellowship NRFF12-2020-0012. Z.D. acknowledges the support from his Lee Kuan Yew Postdoctoral Fellowship 22-5930-A0001. The authors acknowledge the support from the NUS IT Research Computing group (https://nusit.nus.edu.sg). The authors thank the support provided by Dr. Miguel Dias Costa and Dr. Wang Junhong. This work used the computational resources of the supercomputer Fugaku provided by the RIKEN Centre for Computational Science under the "Fugaku Projects via National Supercomputing Centre Singapore," and through the HPCI System Research Project (Project ID: hp230188). The authors acknowledge that the cloud resources involved in this research work are partially supported by NUS IT's Cloud Credits for Research Programme. A proportion of the work was performed at the National Supercomputing Centre, Singapore (https://www.nscc.sg). The authors thank Prof. S. G. Gopalakrishnan at the Indian Institute of Science (Bangalore) for his valuable insights on some aspects of this manuscript.

Conflict of Interest

The authors declare no conflict of interest.

Data Availability Statement

The data that support the findings of this study are openly available in project_grainboundary at https://github.com/caneparesearch/project_grainboundary, reference number 1.

Keywords

electronic properties, first-principles calculations, grain boundaries, mechanical properties, solid electrolytes, surfaces

Received: December 8, 2023
Revised: January 1, 2024
Published online:

[1] R. Van Noorden, *Nature* **2014**, *507*, 26.
[2] J. Liu, Z. Bao, Y. Cui, E. J. Dufek, J. B. Goodenough, P. Khalifah, Q. Li, B. Y. Liaw, P. Liu, A. Manthiram, Y. S. Meng, V. R. Subramanian, M. F. Toney, V. V. Viswanathan, M. S. Whittingham, J. Xiao, W. Xu, J. Yang, X.-Q. Yang, J.-G. Zhang, *Nat. Energy* **2019**, *4*, 180.
[3] G. Deysher, P. Ridley, S.-Y. Ham, J.-M. Doux, Y.-T. Chen, E. A. Wu, D. H. S. Tan, A. Cronk, J. Jang, Y. S. Meng, *Mater. Today Phys.* **2022**, *24*, 100679.
[4] P. Albertus, S. Babinec, S. Litzelman, A. Newman, *Nat. Energy* **2017**, *3*, 16.
[5] J. B. Goodenough, Y. Kim, *Chem. Mater.* **2010**, *22*, 587.
[6] T. Famprikis, P. Canepa, J. A. Dawson, M. S. Islam, C. Masquelier, *Nat. Mater.* **2019**, *18*, 1278.
[7] J. C. Bachman, S. Muy, A. Grimaud, H.-H. Chang, N. Pour, S. F. Lux, O. Paschos, F. Maglia, S. Lupart, P. Lamp, L. Giordano, Y. Shao-Horn, *Chem. Rev.* **2016**, *116*, 140.
[8] J. Wolfenstine, J. L. Allen, J. Sakamoto, D. J. Siegel, H. Choe, *Ionics* **2018**, *24*, 1271.
[9] C. Monroe, J. Newman, *J. Electrochem. Soc.* **2005**, *152*, A396.
[10] J. Kasemchainan, S. Zekoll, D. Spencer Jolly, Z. Ning, G. O. Hartley, J. Marrow, P. G. Bruce, *Nat. Mater.* **2019**, *18*, 1105.
[11] F. Han, A. S. Westover, J. Yue, X. Fan, F. Wang, M. Chi, D. N. Leonard, N. J. Dudney, H. Wang, C. Wang, *Nat. Energy* **2019**, *4*, 187.
[12] E. Kazyak, R. Garcia-Mendez, W. S. LePage, A. Sharafi, A. L. Davis, A. J. Sanchez, K.-H. Chen, C. Haslam, J. Sakamoto, N. P. Dasgupta, *Matter* **2020**, *2*, 1025.
[13] J. Qian, W. A. Henderson, W. Xu, P. Bhattacharya, M. Engelhard, O. Borodin, J.-G. Zhang, *Nat. Commun.* **2015**, *6*, 6362.
[14] R. Garcia-Mendez, F. Mizuno, R. Zhang, T. S. Arthur, J. Sakamoto, *Electrochim. Acta* **2017**, *237*, 144.
[15] F. Han, J. Yue, X. Zhu, C. Wang, *Adv. Energy Mater.* **2018**, *8*, 1703644.
[16] L. Porz, T. Swamy, B. W. Sheldon, D. Rettenwander, T. Frömling, H. L. Thaman, S. Berendts, R. Uecker, W. C. Carter, Y.-M. Chiang, *Adv. Energy Mater.* **2017**, *7*, 1701003.
[17] K. Takada, N. Ohta, Y. Tateyama, *J. Inorg. Organomet. Polym. Mater.* **2015**, *25*, 205.
[18] R. W. Rice, *J. Mater. Sci.* **1984**, *19*, 895.
[19] J. J. Mecholsky, S. W. Freimam, R. W. Rice, *J. Mater. Sci.* **1976**, *11*, 1310.
[20] K. J. Kim, M. Balaish, M. Wadaguchi, L. Kong, J. L. M. Rupp, *Adv. Energy Mater.* **2021**, *11*, 2002689.
[21] E. Milan, M. Pasta, *Mater. Futures* **2023**, *2*, 013501.
[22] J. Tan, M. Ye, J. Shen, *Mater. Today Energy* **2021**, *22*, 100858.
[23] H. Vahidi, K. Syed, H. Guo, X. Wang, J. L. Wardini, J. Martinez, W. J. Bowman, *Crystals* **2021**, *11*, 878.
[24] C. Hu, K. Xia, C. Fu, X. Zhao, T. Zhu, *Energy Environ. Sci.* **2022**, *15*, 1406.
[25] R. Jalem, M. L. Holekevi Chandrappa, J. Qi, Y. Tateyama, S. Ping Ong, *Energy Adv.* **2023**, *2*, 2029.
[26] Z. Deng, V. Kumar, F. T. Bölle, F. Caro, A. A. Franco, I. E. Castelli, P. Canepa, Z. W. Seh, *Energy Environ. Sci.* **2022**, *15*, 579.
[27] K. T. Butler, G. Sai Gautam, P. Canepa, *npj Comput. Mater.* **2019**, *5*, 19.
[28] J. A. Dawson, *ACS Mater. Au* **2024**, *4*, 3c00064.
[29] S. Monismith, J. Qu, R. Dingreville, *J. Mech. Phys. Solids* **2022**, *160*, 104791.
[30] Z. Ning, G. Li, D. L. R. Melvin, Y. Chen, J. Bu, D. Spencer-Jolly, J. Liu, B. Hu, X. Gao, J. Perera, C. Gong, S. D. Pu, S. Zhang, B. Liu, G. O.

Hartley, A. J. Bodey, R. I. Todd, P. S. Grant, D. E. J. Armstrong, T. J. Marrow, C. W. Monroe, P. G. Bruce, *Nature* **2023**, *618*, 287.
[31] B. S. Vishnugopi, M. B. Dixit, F. Hao, B. Shyam, J. B. Cook, K. B. Hatzell, P. P. Mukherjee, *Adv. Energy Mater.* **2022**, *12*, 2102825.
[32] C. Yuan, X. Gao, Y. Jia, W. Zhang, Q. Wu, J. Xu, *Nano Energy* **2021**, *86*, 106057.
[33] Z. Ning, D. S. Jolly, G. Li, R. De Meyere, S. D. Pu, Y. Chen, J. Kasemchainan, J. Ihli, C. Gong, B. Liu, D. L. R. Melvin, A. Bonnin, O. Magdysyuk, P. Adamson, G. O. Hartley, C. W. Monroe, T. J. Marrow, P. G. Bruce, *Nat. Mater.* **2021**, *20*, 1121.
[34] H.-K. Tian, Z. Liu, Y. Ji, L.-Q. Chen, Y. Qi, *Chem. Mater.* **2019**, *31*, 7351.
[35] C. Zhu, T. Fuchs, S. A. L. Weber, F. H. Richter, G. Glasser, F. Weber, H.-J. Butt, J. Janek, R. Berger, *Nat. Commun.* **2023**, *14*, 1300.
[36] T. Fuchs, J. Becker, C. G. Haslam, C. Lerch, J. Sakamoto, F. H. Richter, J. Janek, *Adv. Energy Mater.* **2023**, *13*, 2203174.
[37] B. Gao, R. Jalem, Y. Tateyama, *ACS Appl. Mater. Interfaces* **2020**, *12*, 16350.
[38] J. A. Quirk, J. A. Dawson, *Adv. Energy Mater.* **2023**, 2301114.
[39] Y. Song, L. Yang, L. Tao, Q. Zhao, Z. Wang, Y. Cui, H. Liu, Y. Lin, F. Pan, *J. Mater. Chem. A* **2019**, *7*, 22898.
[40] E. J. Cheng, A. Sharafi, J. Sakamoto, *Electrochim. Acta* **2017**, *223*, 85.
[41] X. Liu, R. Garcia-Mendez, A. R. Lupini, Y. Cheng, Z. D. Hood, F. Han, A. Sharafi, J. C. Idrobo, N. J. Dudney, C. Wang, C. Ma, J. Sakamoto, M. Chi, *Nat. Mater.* **2021**, *20*, 1485.
[42] S. Kalnaus, N. J. Dudney, A. S. Westover, E. Herbert, S. Hackney, *Science* **2023**, *381*, eabg5998.
[43] G. Zhao, K. Suzuki, T. Seki, X. Sun, M. Hirayama, R. Kanno, *J. Solid State Chem.* **2020**, *292*, 121651.
[44] K. Homma, M. Yonemura, T. Kobayashi, M. Nagao, M. Hirayama, R. Kanno, *Solid State Ionics* **2011**, *182*, 53.
[45] T. Bernges, T. Böger, O. Maus, P. S. Till, M. T. Agne, W. G. Zeier, *ACS Mater. Lett.* **2022**, *4*, 2491.
[46] S. Seidel, W. G. Zeier, R. Pöttgen, *Z. Kristallogr. - Cryst. Mater.* **2020**, *235*, 0053.
[47] T. Krauskopf, S. P. Culver, W. G. Zeier, *Inorg. Chem.* **2018**, *57*, 4739.
[48] T. Famprikis, Ö. U. Kudu, J. A. Dawson, P. Canepa, F. Fauth, E. Suard, M. Zbiri, D. Dambournet, O. J. Borkiewicz, H. Bouyanfif, S. P. Emge, S. Cretu, J.-N. Chotard, C. P. Grey, W. G. Zeier, M. S. Islam, C. Masquelier, *J. Am. Chem. Soc.* **2020**, *142*, 18422.
[49] T. Krauskopf, S. Muy, S. P. Culver, S. Ohno, O. Delaire, Y. Shao-Horn, W. G. Zeier, *J. Am. Chem. Soc.* **2018**, *140*, 14464.
[50] P. Gorai, T. Famprikis, B. Singh, V. Stevanović, P. Canepa, *Chem. Mater.* **2021**, *33*, 7484.
[51] H.-J. Deiseroth, J. Maier, K. Weichert, V. Nickel, S.-T. Kong, C. Reiner, *Z. Anorg. Allg. Chem.* **2011**, *637*, 1287.
[52] P. R. Rayavarapu, N. Sharma, V. K. Peterson, S. Adams, *J. Solid State Electrochem.* **2012**, *16*, 1807.
[53] M. A. Kraft, S. P. Culver, M. Calderon, F. Böcher, T. Krauskopf, A. Senyshyn, C. Dietrich, A. Zevalkink, J. Janek, W. G. Zeier, *J. Am. Chem. Soc.* **2017**, *139*, 10909.
[54] R. Murugan, V. Thangadurai, W. Weppner, *Angew. Chem., Int. Ed.* **2007**, *46*, 7778.
[55] Z. Deng, G. Sai Gautam, S. K. Kolli, J.-N. Chotard, A. K. Cheetham, C. Masquelier, P. Canepa, *Chem. Mater.* **2020**, *32*, 7908.
[56] H. Y.-P. Hong, *Mater. Res. Bull.* **1976**, *11*, 173.
[57] J. B. Goodenough, H. Y.-P. Hong, J. A. Kafalas, *Mater. Res. Bull.* **1976**, *11*, 203.
[58] T. Asano, A. Sakai, S. Ouchi, M. Sakaida, A. Miyazaki, S. Hasegawa, *Adv. Mater.* **2018**, *30*, 1803075.
[59] S. Wang, Q. Bai, A. M. Nolan, Y. Liu, S. Gong, Q. Sun, Y. Mo, *Angew. Chem., Int. Ed.* **2019**, *58*, 8039.
[60] X. Li, J. Liang, X. Yang, K. R. Adair, C. Wang, F. Zhao, X. Sun, *Energy Environ. Sci.* **2020**, *13*, 1429.
[61] E. Sebti, H. A. Evans, H. Chen, P. M. Richardson, K. M. White, R. Giovine, K. P. Koirala, Y. Xu, E. Gonzalez-Correa, C. Wang, C. M. Brown, A. K. Cheetham, P. Canepa, R. J. Clément, *J. Am. Chem. Soc.* **2022**, *144*, 5795.
[62] Y. Zhu, X. He, Y. Mo, *ACS Appl. Mater. Interfaces* **2015**, *7*, 23685.
[63] W. D. Richards, L. J. Miara, Y. Wang, J. C. Kim, G. Ceder, *Chem. Mater.* **2016**, *28*, 266.
[64] S. Yu, D. J. Siegel, *Chem. Mater.* **2017**, *29*, 9639.
[65] P. Barai, K. Higa, A. T. Ngo, L. A. Curtiss, V. Srinivasan, *J. Electrochem. Soc.* **2019**, *166*, A1752.
[66] P. W. Tasker, *J. Phys. C: Solid State Phys.* **1979**, *12*, 4977.
[67] N. L. Marana, M. F. Sgroi, L. Maschio, A. M. Ferrari, M. D'Amore, S. Casassa, *Nanomaterials* **2022**, *12*, 2795.
[68] L. E. Camacho-Forero, P. B. Balbuena, *Chem. Mater.* **2020**, *32*, 360.
[69] P. Canepa, J. A. Dawson, G. Sai Gautam, J. M. Statham, S. C. Parker, M. S. Islam, *Chem. Mater.* **2018**, *30*, 3019.
[70] P. P. Ewald, *Ann. Phys.* **1921**, *369*, 253.
[71] S. P. Ong, W. D. Richards, A. Jain, G. Hautier, M. Kocher, S. Cholia, D. Gunter, V. L. Chevrier, K. A. Persson, G. Ceder, *Comput. Mater. Sci.* **2013**, *68*, 314.
[72] N. Bozzolo, M. Bernacki, *Metall. Mater. Trans. A* **2020**, *51*, 2665.
[73] F. Zheng, L. Huang, L.-W. Wong, J. Han, Y. Cai, N. Wang, Q. Deng, T. H. Ly, J. Zhao, *Adv. Sci.* **2020**, *7*, 2001742.
[74] J. A. Dawson, P. Canepa, T. Famprikis, C. Masquelier, M. S. Islam, *J. Am. Chem. Soc.* **2018**, *140*, 362.
[75] A. R. Symington, M. Molinari, J. A. Dawson, J. M. Statham, J. Purton, P. Canepa, S. C. Parker, *J. Mater. Chem. A* **2021**, *9*, 6487.
[76] F. Iguchi, T. Yamada, N. Sata, T. Tsurui, H. Yugami, *Solid State Ionics* **2006**, *177*, 2381.
[77] S. von Alfthan, N. A. Benedek, L. Chen, A. Chua, D. Cockayne, K. J. Dudeck, C. Elsässer, M. W. Finnis, C. T. Koch, B. Rahmati, M. Rühle, S.-J. Shih, A. P. Sutton, *Annu. Rev. Mater. Res.* **2010**, *40*, 557.
[78] F. Ernst, M. L. Mulvihill, O. Kienzle, M. Rühle, *J. Am. Ceram. Soc.* **2004**, *84*, 1885.
[79] R. Kurtz, H. Heinisch, *J. Nucl. Mater.* **2004**, *329–333*, 1199.
[80] G. S. Rohrer, *J. Mater. Sci.* **2011**, *46*, 5881.
[81] S. Ratanaphan, D. Raabe, R. Sarochawikasit, D. L. Olmsted, G. S. Rohrer, K. N. Tu, *J. Mater. Sci.* **2017**, *52*, 4070.
[82] C. Liu, Z. G. Neale, G. Cao, *Mater. Today* **2016**, *19*, 109.
[83] T. Famprikis, H. Bouyanfif, P. Canepa, M. Zbiri, J. A. Dawson, E. Suard, F. Fauth, H. Y. Playford, D. Dambournet, O. J. Borkiewicz, M. Courty, O. Clemens, J.-N. Chotard, M. S. Islam, C. Masquelier, *Chem. Mater.* **2021**, *33*, 5652.
[84] T. Krauskopf, S. P. Culver, W. G. Zeier, *Chem. Mater.* **2018**, *30*, 1791.
[85] T. Thompson, S. Yu, L. Williams, R. D. Schmidt, R. Garcia-Mendez, J. Wolfenstine, J. L. Allen, E. Kioupakis, D. J. Siegel, J. Sakamoto, *ACS Energy Lett.* **2017**, *2*, 462.
[86] M. D'Amore, L. Edith Daga, R. Rocca, M. Francesco Sgroi, N. Leticia Marana, S. Maria Casassa, L. Maschio, A. Maria Ferrari, *Phys. Chem. Chem. Phys.* **2022**, *24*, 22978.
[87] L. Shvindlerman, G. Gottstein, *Scr. Mater.* **2006**, *54*, 1041.
[88] E. Bakir Kandemir, B. Gönül, G. T. Barkema, K. M. Yu, W. Walukiewicz, L. W. Wang, *Comput. Mater. Sci.* **2014**, *82*, 100.
[89] P. A. Anderson, *Phys. Rev.* **1949**, *75*, 1205.
[90] A. Kato, H. Kowada, M. Deguchi, C. Hotehama, A. Hayashi, M. Tatsumisago, *Solid State Ionics* **2018**, *322*, 1.
[91] N. D. Lepley, N. A. W. Holzwarth, Y. A. Du, *Phys. Rev. B* **2013**, *88*, 104103.
[92] Y. Nikodimos, W.-N. Su, B. J. Hwang, *Adv. Energy Mater.* **2023**, *13*, 2202854.
[93] W. Ji, D. Zheng, X. Zhang, T. Ding, D. Qu, *J. Mater. Chem. A* **2021**, *9*, 15012.

[94] L. M. Riegger, R. Schlem, J. Sann, W. G. Zeier, J. Janek, *Angew. Chem., Int. Ed. Engl.* **2021**, *60*, 6718.
[95] S. Wenzel, S. J. Sedlmaier, C. Dietrich, W. G. Zeier, J. Janek, *Solid State Ionics* **2018**, *318*, 102.
[96] D. Cheng, T. A. Wynn, X. Wang, S. Wang, M. Zhang, R. Shimizu, S. Bai, H. Nguyen, C. Fang, M.-c. Kim, W. Li, B. Lu, S. J. Kim, Y. S. Meng, *Joule* **2020**, *4*, 2484.
[97] L. E. Goodwin, P. Till, M. Bhardwaj, N. Nazer, P. Adelhelm, F. Tietz, W. G. Zeier, F. H. Richter, J. Janek, *ACS Appl. Mater. Interfaces* **2023**, *15*, 50457.
[98] T. Ortmann, S. Burkhardt, J. K. Eckhardt, T. Fuchs, Z. Ding, J. Sann, M. Rohnke, Q. Ma, F. Tietz, D. Fattakhova-Rohlfing, C. Kübel, O. Guillon, C. Heiliger, J. Janek, *Adv. Energy Mater.* **2023**, *13*, 2202712.
[99] J. Wang, A. A. Panchal, G. Sai Gautam, P. Canepa, *J. Mater. Chem. A* **2022**, *10*, 19732.
[100] L. Lin, X. Wang, X. Zeng, *Int. J. Damage Mech.* **2017**, *26*, 379.
[101] R. H. Kraft, J. F. Molinari, *Acta Mater.* **2008**, *56*, 4739.
[102] P. F. Becher, *J. Am. Ceram. Soc.* **1991**, *74*, 255.
[103] O. A. Shenderova, D. W. Brenner, A. Omeltchenko, X. Su, L. H. Yang, *Phys. Rev. B* **2000**, *61*, 3877.
[104] A. S. Kobayashi, *Mater. Sci. Eng., A* **1991**, *143*, 111.
[105] E. A. Holm, J. H. Meinke, E. S. McGarrity, P. M. Duxbury, *Mater. Sci. Forum* **2004**, *467–470*, 1039.
[106] D. Tromans, J. A. Meech, *Miner. Eng.* **2004**, *17*, 1.
[107] *Fracture of Brittle Solids*, 2nd ed., (Ed. B. Lawn), Cambridge Solid State Science Series, Cambridge University Press, Cambridge **1993**, pp. 16–50.
[108] W. Zhang, J. Nie, F. Li, Z. L. Wang, C. Sun, *Nano Energy* **2018**, *45*, 413.
[109] S. Yu, D. J. Siegel, *ACS Appl. Mater. Interfaces* **2018**, *10*, 38151.
[110] J. E. Ni, E. D. Case, J. S. Sakamoto, E. Rangasamy, J. B. Wolfenstine, *J. Mater. Sci.* **2012**, *47*, 7978.
[111] A. Sharafi, C. G. Haslam, R. D. Kerns, J. Wolfenstine, J. Sakamoto, *J. Mater. Chem. A* **2017**, *5*, 21491.
[112] J. Wolfenstine, H. Jo, Y.-H. Cho, I. N. David, P. Askeland, E. D. Case, H. Kim, H. Choe, J. Sakamoto, *Mater. Lett.* **2013**, *96*, 117.
[113] H. Guo, J. Su, W. Zha, T. Xiu, Z. Song, M. E. Badding, J. Jin, Z. Wen, *J. Alloys Compd.* **2021**, *856*, 157222.
[114] S. Hu, P. Xu, L. S. De Vasconcelos, L. Stanciu, H. Ni, K. Zhao, *Chin. Phys. Lett.* **2021**, *38*, 098401.
[115] A. P. Sutton, *Philos. Mag. A* **1991**, *63*, 793.
[116] K. J. Kim, M. Balaish, M. Wadaguchi, L. Kong, J. L. M. Rupp, *Adv. Energy Mater.* **2021**, *11*, 2002689.
[117] H. Hayashi, T. Ebina, *J. Ceram. Soc. Jpn.* **2018**, *126*, 214.
[118] R. Pfenninger, M. Struzik, I. Garbayo, E. Stilp, J. L. M. Rupp, *Nat. Energy* **2019**, *4*, 475.
[119] R. Koerver, I. Aygün, T. Leichtweiß, C. Dietrich, W. Zhang, J. O. Binder, P. Hartmann, W. G. Zeier, J. Janek, *Chem. Mater.* **2017**, *29*, 5574.
[120] C. E. Athanasiou, C. D. Fincher, C. Gilgenbach, H. Gao, W. C. Carter, Y.-M. Chiang, B. W. Sheldon, *Matter* **2023**, *7*, 95.
[121] M. L. Jokl, V. Vitek, C. J. McMahon, *Acta Metall.* **1980**, *28*, 1479.
[122] X. Tingdong, Z. Lei, *Philos. Mag. Lett.* **2004**, *84*, 225.
[123] O. Yeheskel, R. Chaim, Z. Shen, M. Nygren, *J. Mater. Res.* **2005**, *20*, 719.
[124] M. W. Barsoum, *Fundamentals of Ceramics*, 2nd ed., CRC Press, Boca Raton, FL **2019**.
[125] L. Zhang, T. Yang, C. Du, Q. Liu, Y. Tang, J. Zhao, B. Wang, T. Chen, Y. Sun, P. Jia, H. Li, L. Geng, J. Chen, H. Ye, Z. Wang, Y. Li, H. Sun, X. Li, Q. Dai, Y. Tang, Q. Peng, T. Shen, S. Zhang, T. Zhu, J. Huang, *Nat. Nanotechnol.* **2020**, *15*, 94.
[126] K. Leung, K. L. Jungjohann, *J. Phys. Chem. C* **2017**, *121*, 20188.
[127] Y. Dong, F. Wang, W. Lai, *Int. J. Hydrogen Energy* **2017**, *42*, 10124.
[128] T. Uesugi, K. Higashi, *J. Mater. Sci.* **2011**, *46*, 4199.
[129] S. Pal, K. V. Reddy, T. Yu, J. Xiao, C. Deng, *J. Mater. Sci.* **2021**, *56*, 11511.
[130] S. Zhang, O. Y. Kontsevoi, A. J. Freeman, G. B. Olson, *Phys. Rev. B* **2011**, *84*, 134104.
[131] J. P. Perdew, K. Burke, M. Ernzerhof, *Phys. Rev. Lett.* **1996**, *77*, 3865.
[132] G. Kresse, J. Furthmüller, *Phys. Rev. B* **1996**, *54*, 11169.
[133] P. E. Blöchl, *Phys. Rev. B* **1994**, *50*, 17953.
[134] G. Kresse, D. Joubert, *Phys. Rev. B* **1999**, *59*, 1758.